Thermoelectric Performance and Defect Chemistry in n-Type Zintl KGaSb₄

Brenden R. Ortiz,*,[†] Prashun Gorai,[‡] Vladan Stevanović,[‡,§] and Eric S. Toberer*,[†,‡]

[†]Department of Physics, Colorado School of Mines, Golden, Colorado 80401, United States

[‡]National Renewable Energy Laboratory, Golden, Colorado 80401, United States

[§]Department of Metallurgy, Colorado School of Mines, Golden, Colorado 80401, United States

Ⓢ Supporting Information

ABSTRACT: The rise of high-throughput calculations has accelerated the discovery of promising classes of thermoelectric materials. In prior work, we identified the n-type Zintl pnictides as one such material class. To date, however, a lack of detailed defect calculations and chemical intuition has led the community to investigate p-type Zintls almost exclusively. Here, we investigate the synthesis, thermoelectric properties, and defect structure of the complex Zintl KGaSb₄. We find that KGaSb₄ is successfully doped n-type with Ba and has the potential for p-type doping with Zn. Our calculations reveal the fundamental defect structure in KGaSb₄ that enables n-type and p-type doping. We find that Ba doped KGaSb₄ exhibits high electronic mobility (~50 cm²V⁻¹s⁻¹) and near minimum lattice thermal conductivity (<0.5 Wm⁻¹K⁻¹) at 400 °C. Samples doped with 1.5% Ba achieve $zT > 0.9$ at 400 °C, promising for a previously unstudied material. We also briefly investigate the series of alloys between KGaSb₄ and KAlSb₄, finding that a full solid solution exists. Altogether our work reinforces motivation for the exploration of n-type Zintl materials, especially in tandem with high-throughput defect calculations to inform selection of effective dopants and systems amenable to n-type transport.
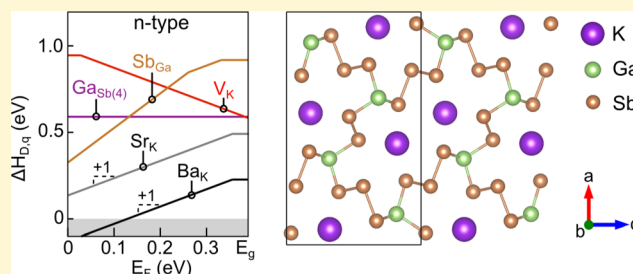
INTRODUCTION

The discovery of new materials with a high thermoelectric figure of merit zT would represent a great addition to the global energy portfolio.[1−3] Historically, however, the pursuit of new thermoelectric materials has been driven by experimental work and chemical intuition. Recent years have seen the integration of high-throughput computation to aid the discovery of new material classes and novel thermoelectric materials.[4−9] For example, we have previously developed a metric for quantifying the thermoelectric potential of a material based on the quality factor β.[10] Our metric can be evaluated directly from first-principles calculations and semiempirical models in a computationally tractable, high-throughput fashion.[9]

However, the mere discovery of new materials is insufficient to develop practical thermoelectric devices. The application of a new system depends critically on its ability to be optimized and doped. Doping, in particular, poses a significant challenge to the thermoelectric community, as the transport properties entering zT depend on the carrier concentration in multiple, conflicting ways. Optimized materials commonly have carrier concentrations in the $10^{19}-10^{20}$ cm⁻³ range, which often requires the intentional doping of intrinsic materials (e.g., PbTe,[11] SnS[12]) compensated doping in degenerate materials (e.g., SnTe,[13] Yb₁₄MnSb₁₁,[14] Cu₂Se[15]). The identification of successful dopants is currently dominated by experimental trial-and-error, a time-consuming and laborious process. Further, the

analysis of successful dopants is relatively simple, leaving results to be interpreted with chemical intuition alone.

The capabilities of first-principles defect calculations have increased dramatically in the past 10 years.[16,17] Other facets of material science (e.g., battery research and photovoltaics) have begun using first-principles defect calculations with resounding success.[18−20] With the onus thermoelectrics places on doping, the application of defect calculations seems a natural extension. Accordingly, several instances of first-principles defect calculations in thermoelectrics have begun to emerge.[21,22] Our ultimate goal is to combine the identification of promising systems (via β, semiempirical models, and high-throughput calculations) with high-throughput defect calculations to accelerate the development of next generation thermoelectrics. This work, combined with our prior work on KAlSb₄,[23] represents our first union of promising material identification[9,23] with defect calculations to accelerate material development.

In our prior work, we performed calculations on 145 Zintl pnictides (a vetted class of p-type thermoelectric materials, known for their exceptionally low thermal conductivity).[23] We found that the number of promising n-type Zintls materials outnumber and possibly outperform the p-type counterparts.

Characterized by high electron mobilities (>100 cm^{2}V^{-1}s^{-1}) *and* exceptionally low thermal conductivity, the n-type Zintls proved to be a promising, unexplored family of materials. Previously, we began to validate our computational search by synthesizing n-type KAlSb$_4$, a previously unstudied material with a peak *zT* of 0.7.[23] KAlSb$_4$ was one of the few discoveries of an n-type Zintl.[24,25] It is not clear whether the lack of n-type materials is related to a deeper phenomenon or synthetic bias toward the p-type Zintl compounds, and our prior work did not seek to investigate the source of the n-type transport.

In this work, we seek to understand the source of n-type dopability in some Zintl materials using first-principles defect structure calculations. We have chosen KGaSb$_4$ as the model system for this study, due to its chemical and structural similarity to KAlSb$_4$, as well as its predicted properties exceeding those of KAlSb$_4$. The material is isostructural with KAlSb$_4$, although KGaSb$_4$ exhibits a significantly smaller cell volume. To our knowledge, KAlSb$_4$ and KGaSb$_4$ are the only known materials that possess this structure type. Figure 1 shows
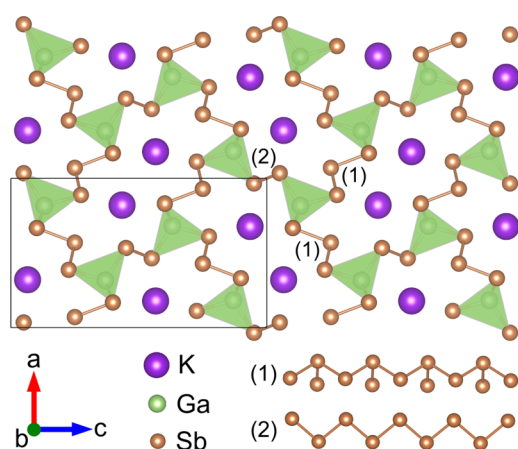
Figure 1. The crystal structure of KGaSb$_4$ is isostructural to KAlSb$_4$ and is comprised of inifinte chains of corner-sharing GaSb$_4$ tetrahedra extending in the *b*-direction. The chains of GaSb$_4$ tetrahedra are interconnected by two chains of trigonal pyramidal Sb chains (1) and one zigzag chain (2). The structure creates infinite channels of K ions parallel to the *b*-direction.

the crystal structure and extended bonding of KGaSb$_4$.[26] The structure is reminiscent of BaGa$_2$Sb$_2$, which also contains channels of Ba atoms surrounded by an anionic framework of Ga–Sb.[27,28] Prior work was limited to the original structural study, wherein the material was synthesized for the first time from its constituent elements at 650 °C.[26]

Here we present the synthesis, thermoelectric properties, and defect energetics of Ba-doped KGaSb$_4$. The synthesis is conducted via high-energy ball milling followed by uniaxial hot-pressing to yield dense, single phase ingots. A combination of X-ray diffraction, electron microscopy, and Hall effect measurements are utilized to determine the solubility limit of Ba in KGaSb$_4$. High temperature resistivity, Seebeck coefficient, and thermal diffusivity measurements are used to reveal the electronic and thermal transport properties of KGaSb$_4$. First-principles defect structure calculations are used to investigate the primary intrinsic defects in KGaSb$_4$, as well as investigate the effectiveness of several n-type and p-type dopants in KGaSb$_4$. Overall, Ba doped KGaSb$_4$ proves to be a promising material with *zT* > 0.9 at 400 °C. We also briefly discuss the series of alloys between KGaSb$_4$ and KAlSb$_4$ in order to

investigate the effect of alloying on the thermoelectic potential of this system.

■ METHODS

Experimental Section. Samples of K$_{1-x}$Ba$_x$GaSb$_4$ ($0 \leq x \leq 0.025$) are synthesized through high-energy ball milling followed by reactive uniaxial hot-pressing. All sample preparation, measuring of raw reagents, and handling of powders is performed in an argon drybox with an oxygen concentration <1 ppm. Unlike our prior work on KAlSb$_4$ (synthesized off stoichiometry as KAlSb$_{3.8}$ to suppress Sb impurities),[23] samples of KGaSb$_4$ are synthesized under near stoichiometric conditions (KGaSb$_{3.98}$). The minor Sb deficiency intentionally generates a small amount (<2 vol %) of KGaSb$_2$ which pins all samples to the same impurity phase within the K–Ga–Sb phase space. For the alloying series, K$_{0.99}$Ba$_{0.01}$Al$_{1-x}$Ga$_x$Sb$_4$ samples were synthesized under Sb-poor conditions, similar to those in our prior work on KAlSb$_4$.[23]

For the Ba-doping of KGaSb$_4$, elemental gallium metal (Alfa 99.999%) liquefied at 50 °C is loaded with antimony shot (Alfa 99.999%) and barium shavings taken from a barium rod (Alfa 99+%) into a tungsten carbide ball mill vial with two 7/16″ tungsten carbide balls. The mixture is milled for 30 min to prereact the gallium and evenly disperse the barium dopant. A potassium chunk (Alfa 99.5%) is cleaned by cutting deeply into the ingot to reveal clean metal and is then added to the Ba–Ga–Sb mixture. The mixture is milled in a high-energy SPEX 8000D mill for 10 cycles of duration 1 min. The vial is rotated between each cycle to prevent excessive adhesion of powder to bottom and walls of vial. The walls and end-caps of the vial are scraped halfway through the mill process (after 5 cycles) to dislodge any stuck material. Powders are subsequently ground in an agate mortar and doubly sieved through a 106 μm mesh adhering to ASTM E11 standards. The alloying series follows a similar procedure, with the addition of finely divided elemental aluminum shot (Alfa 99.999%) to the Ba–Ga–Sb mixture prior to K addition. Furthermore, milling of the Ba-Al–Ga-Sb mixture is increased to 60 min to ensure homogeneity of powder.

Polycrystalline ingots of K$_{1-x}$Ba$_x$GaSb$_4$ are formed via reactive hot pressing in a high-density graphite die under dynamic vacuum. Prior to use, the graphite die, plungers, and graphite foil liners are baked at 600 °C for a minimum of 30 min under dynamic vacuum. Approximately 5.25 g of milled powder is loaded into the cooled die and transferred to the hot press chamber. The chamber is evacuated to <5 mTorr and purged with argon to ∼0.75 Atm thrice before finally evacuating the chamber to <1 mTorr. Twenty-five MPa of pressure are applied to the sample to achieve a rough green body density before relieving the pressure to 15 MPa and beginning the temperature profile. The sample is quickly heated to 300 °C at 20 °C/min. The heating rate is subsequently slowed to 0.15 °C/min from 300 to 350 °C, during which the sample undergoes densification at a linear rate. Afterward, the sample is heated to 525 °C at 20 °C/min and held at 525 °C for 12 h. The sample cools from 525 °C at a controlled rate of 20 °C/min. To increase clarity with regard to the hot-pressing procedure, a simplified schematic of a typical press cycle is included in the Supporting Information, Figure S1. Hot-pressing procedures for the alloying series follows a similar profile.

Resulting ingots are sectioned into 2.5 mm thick discs in a Buehler slow cut saw. Samples are polished using a series of carbide sandpaper and diamond grits to ∼1 μm. Light mineral oil is used as the grinding liquid as our observations indicate that KGaSb$_4$ is mildly reactive with liquid water and some solvents. While KAlSb$_4$ will tarnish in air, polished samples of KGaSb$_4$ are remarkably stable in air, retaining their luster and electronic properties after exposure to ambient for >3 weeks. Sample densities are measured by the geometrical method and are consistently >97% of the density predicted by X-ray diffraction. Sample densities for the alloying series are marginally lower, but still >95% of the density predicted by XRD.

X-ray diffraction (XRD) patterns are collected on a Bruker D2 Phaser diffractometer in a θ-2θ configuration using Cu Kα radiation. Rietveld refinement of KGaSb$_4$ patterns utilized pure KGaSb$_4$ (ICSD:

300158) as the base pattern and the GSAS II software package.[29] Refinement of the alloyed samples used a custom CIF file based on the KAlSb$_4$ (ICSD: 300157) and KGaSb$_4$ (ICSD: 300158) structures with Al−Ga occupancies matching the nominal concentration of Al and Ga. For all samples, refined parameters include: lattice parameters, isotropic domain size, atomic positions, and microstrain. We do not attempt to refine atomic occupancy or thermal parameters with current XRD data. Instrumental parameters are refined using a NIST LaB$_6$ sample to increase the fidelity of results. Energy dispersive spectroscopy (EDS) of polished surfaces is performed on a FEI Quanta 600i Scanning Electron Microscope (SEM).

Hall effect and resistivity measurements are performed using the Van der Pauw geometry on home-built apparatus.[30] Measurements are conducted up to 400 °C under dynamic vacuum (<10^{-4} Torr). Contacts are pressure-assisted nichrome wire. After contacts are established, samples are coated with boron nitride spray to suppress sublimation. To allow contact annealing and bake-out of the boron nitride coating, samples undergo one thermal cycle under dynamic vacuum before transport data is taken. Seebeck coefficient measurements were conducted using the quasi-steady slope method up to 400 °C under high vacuum (<10^{-6} Torr).[30,31] Boron nitride coating is removed before Seebeck effect measurements are made. We note that samples of KGaSb$_4$ are more resistant to thermal degradation than KAlSb$_4$, and may not require the boron nitride coating up to 400 °C.

Thermal diffusivity is measured using a Netzsch Laser Flash Apparatus (LFA) 457, and the resulting diffusivity data are fit using a Cowen plus Pulse Correction (CPC) numerical model. The samples are coated with graphite spray prior to measurement to reduce errors in sample emissivity. The total thermal conductivity of the alloyed samples is calculated using the following:

$$\kappa = D\rho C_p \tag{1}$$

where D is the thermal diffusivity, ρ is the mass density, and C_p is the volumetric heat capacity. The heat capacity is estimated using the Dulong−Petit approximation.

Speed of sound measurements are performed using an Olympus 5072PR Pulser/Receiver system with a gain of 20 dB and a 5 kHz signal. Both longitudinal and shear measurements were made, using Olympus V112 (longitudinal) and Olympus V156 (shear) transducers and an Atten ADS 1102 oscilloscope.

We note that samples of KGaSb$_4$ are visually unchanged after Hall, Seebeck, and thermal diffusivity measurements. Surfaces are still lustrous after boron nitride or graphite spray are removed with a kimwipe and mineral oil. The alloying series displays similar results, although signs of sublimation are evident near the Al-rich side, consistent with observations from our prior work on KAlSb$_4$.[23]

Computational. To understand the native defect chemistry of KGaSb$_4$ and to assess the effectiveness of several n- and p-type extrinsic dopants, we performed first-principles defect calculations with density functional theory (DFT) using the VASP software package.[32] The generalized gradient approximation (GGA) of Perdew−Burke−Ernzerhof (PBE)[33] in the projector augmented wave formalism[34] was used. Total energies of defect supercells containing 192 atoms were calculated with a plane-wave cutoff of 340 eV and a Γ-centered Monkhorst pack k-point grid of 4 × 4 × 4. The defect supercells were relaxed following the procedure outlined in ref 35. The defect formation enthalpies ($\Delta H_{D,q}$) are calculated from the total energies as follows:

$$\Delta H_{D,q}(E_F, \mu) = (E_{D,q} - E_H) + \sum_i n_i\mu_i + qE_F + E_{corr} \tag{2}$$

where $E_{D,q}$ and E_H are the total energies of the defect and host supercell, respectively. μ_i is the chemical potential of elemental species i added ($n_i < 0$) or removed ($n_i > 0$) from the host supercell to form the defect. E_F is the Fermi energy, and E_{corr} comprises all the finite-size corrections, within the supercell approach. The chemical potentials μ_i are expressed relative to the reference elemental phase such that $\mu_i = \mu_i^0 + \Delta\mu_i$, where μ_i^0 is the reference elemental chemical potential calculated using FERE[35] and $\Delta\mu_i$ is the deviation from the reference

elemental phase. The bounds on $\Delta\mu_i$ are set by the region of phase stability, and $\Delta\mu_i = 0$ corresponding to i-rich conditions.

The DFT-GGA band gap underestimation was "corrected" by applying band edge shifts determined from GW quasi-particle energy calculations, as described in ref 36. The band edge shifts for KGaSb$_4$ are $\Delta E_{VBM} = -0.1$ eV and $\Delta E_{CBM} = 0.04$ eV. The resultant band gap, after application of GW shifts, is 0.39 eV. The following corrections were included in E_{corr} following the methodology in ref 37: (1) image charge correction for charged defects, (2) potential alignment correction for charged defects, (3) band filling correction for shallow defects, and (4) band gap correction for shallow donors/acceptors. The calculation setup and analyses were performed using a software package that we have recently developed for automation of defect calculations.[16]

In KGaSb$_4$, K and Ga atoms each occupy a unique Wyckoff position while Sb occupies 4 different Wyckoff positions. Therefore, 6 different vacancies (V_K, V_{Ga}, V_{Sb1}, V_{Sb2}, V_{Sb3}, and V_{Sb4}) and 5 antisites (Ga$_{Sb1}$, Ga$_{Sb2}$, Ga$_{Sb3}$, Ga$_{Sb4}$, and Sb$_{Ga}$) were considered as native defects in 7 different charge states $q = -3, -2, -1, 0, 1, 2,$ and 3. The numbers in the subscripts denote unique Wyckoff positions. Preliminary examination of K antisites with Ga and Sb revealed high defect formation energies and were therefore not considered in the set of possible native defects. Extrinsic dopants Ba, Sr, and Zn were considered as substitutional defects on all sites (K, Ga, and Sb) in 7 different charge states $q = -3, -2, -1, 0, 1, 2,$ and 3.

The bounds on $\Delta\mu_i$ corresponding to the region of phase stability of KGaSb$_4$ are obtained from the National Renewable Energy Laboratory (NREL) Materials Database (materials.nrel.gov). The ternary phase stability region of KGaSb$_4$ is rather narrow such that $\Delta\mu_i$ of K, Ga, and Sb do not vary significantly in different parts of the stability region. The same is true when considering the quaternary phase stability region involving extrinsic dopants Ba, Sr, and Zn. The defect diagrams ($\Delta H_{D,q}$ vs E_F) are all calculated at one point in the phase stable region where $\Delta\mu_{Sb} = 0$ (Sb-rich). The position of the pinned Fermi level, the corresponding defect/dopant concentrations, and the free carrier concentrations at a given temperature were calculated self-consistently by establishing charge neutrality. The defect/dopant concentrations were calculated using the Boltzmann relation.

RESULTS AND DISCUSSION

Structure and Composition. Our synthesis procedure yields dense (>97% theoretical density) discs of KGaSb$_4$. The crystal structure and phase purity of sintered K$_{1-x}$Ba$_x$GaSb$_4$ samples was assessed by X-ray diffraction (XRD) and subsequent Rietveld refinement. Figure 2 shows a typical XRD diffraction pattern collected on pure KGaSb$_4$ and refined using ICSD pattern 300158. Additional XRD results for the doping series can be found in Figure S2. For all hot-pressed samples, we identify a small (<2 vol %) amount of KGaSb$_2$. An additional impurity phase appears in samples containing Ba in concentrations $x \geq 0.020$. Due to the extremely low intensities, this phase cannot be reliably indexed by XRD, but is most likely Ba$_3$GaSb$_3$. Appearance of secondary phase suggests termination of solid-solution around Ba $x \approx 0.020$. However, due to the similar ionic radii of Ba^{2+} and K$^+$ and the generally low concentration of Ba, no trend is observed in the lattice parameters or cell volume.

Energy dispersive spectroscopy (EDS) mapping of sample surfaces confirms phase purity in samples with Ba $x \leq 0.015$ and simultaneously confirms the appearance of small (~1 μm) roughly spherical precipitates in samples with Ba $x \geq 0.020$. The precipitates comprise an extremely minor fraction of the total scanned area; their composition cannot be resolved against the KGaSb$_4$ host matrix. Within the error of standardless EDS, the average composition of each sample is consistent with the nominal stoichiometry of KGaSb$_4$. Barium
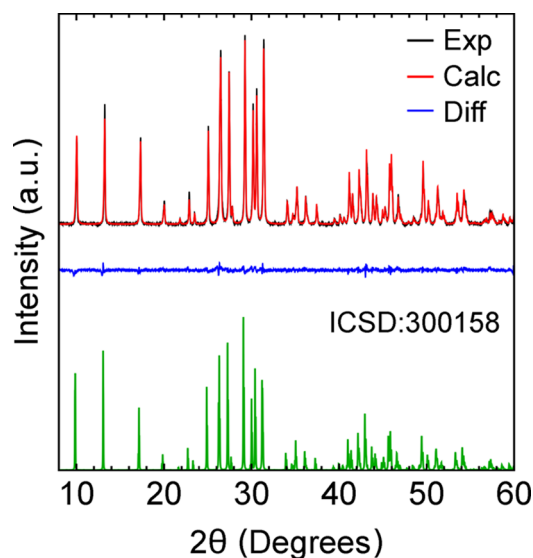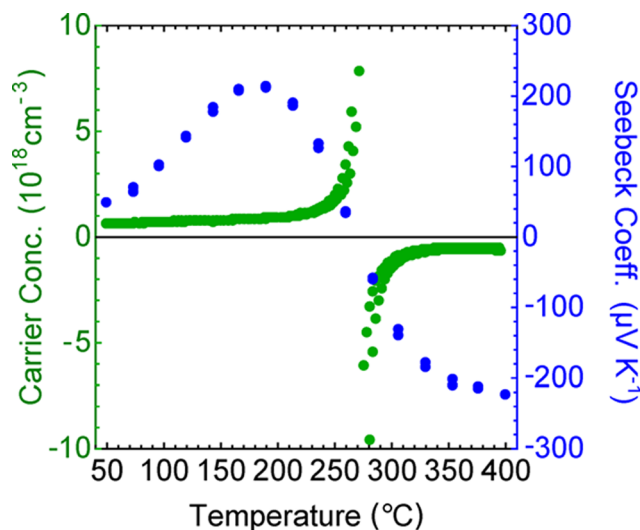
Figure 2. Representative Rietveld refinement (red) of the $KGaSb_4$ diffraction pattern (black) and associated difference profile (blue). Reference diffraction pattern (ICSD: 300158) is shown for comparison. Rietveld indicates that material is >98% phase pure with a trace amount of $KGaSb_2$. Minor texturing is evident in all samples.

Figure 3. High temperature Seebeck coefficient (blue) and Hall carrier concentration (green) measurements on undoped $KGaSb_4$ confirm intrinsic transport. Bipolar transport strongly contributes to the functional form of both the Seebeck coefficient and Hall carrier concentration over all temperatures. Note that carrier concentrations are $<10^{17}$ cm^{-3} over all temperatures; the steep curvature near the transition at 275 °C is an artifact of the Hall voltage switching sign and the subsequent calculation of the Hall carrier concentration.

concentration is not well resolved due to the low concentration of the dopant. EDS results are provided in Table S1.
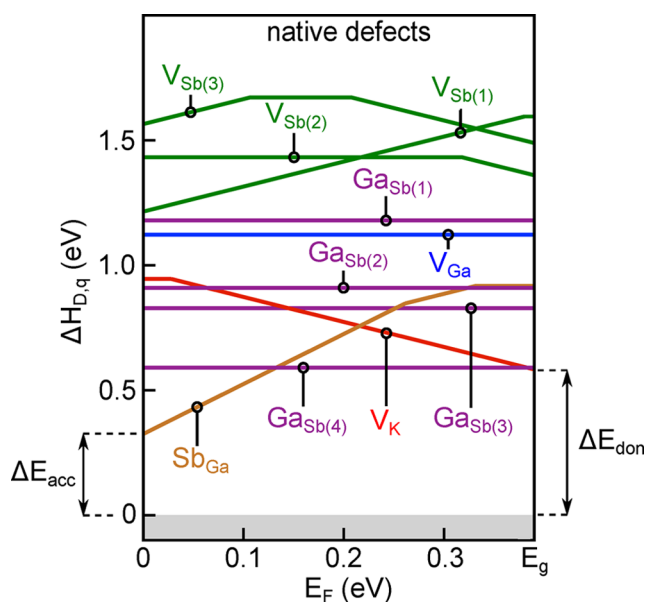
Intrinsic Transport and Native Defects. Commonly held intuition within the thermoelectric community dictates that Zintl compounds are commonly p-type due to the proclivity of alkali and alkali earth vacancy formation. Experimentally, however, we find that undoped $KGaSb_4$ exhibits properties consistent with an intrinsic semiconductor. Figure 3 shows the high temperature Seebeck coefficient and Hall carrier concentration measurements for undoped $KGaSb_4$.

Both the high temperature Seebeck coefficient and Hall carrier concentration demonstrate a strong contribution from thermally activated bipolar transport. Intrinsic $KGaSb_4$ is a weakly p-type material until 275 °C, where a sharp transition to n-type transport is observed. It is important to note that carrier concentrations are in the $10^{17} cm^{-3}$ range for all temperatures. The curvature of the Hall effect data near the thermal transition point is formally an artifact of the Hall voltage switching signs and the breakdown of the single carrier type approximation within typical Hall analysis.

Despite intuition suggesting that potassium vacancies V_K should be the dominant defect, our experimental results indicate that either (i) there are compensating defects that pin the Fermi level in the mid gap region resulting in intrinsic transport behavior, or (ii) the native defects have high formation energies. To better understand the defect chemistry in $KGaSb_4$, we have performed first-principles DFT calculations to determine the native defect formation enthalpies $\Delta H_{D,q}$. Figure 4 shows the plot of $\Delta H_{D,q}$ as a function of the Fermi level (E_F) for 10 different native defects in $KGaSb_4$ under Sb-rich conditions. We stress that our computations indicate that $KGaSb_4$ is stable under a very narrow range of chemical potentials, such that our calculations are valid over all experimentally accessible compositions. The native defects considered include vacancies and antisites (see the Methods section for computational details). The line slope is equal to the defect charge state.

Figure 4. Formation enthalpy $\Delta H_{D,q}$ as a function of Fermi level E_F for 10 different native defects, including vacancies (e.g., V_K) and antisites (e.g., Sb_{Ga}) in $KGaSb_4$ under Sb-rich conditions. E_F varies from zero (top of the valence band) to the band gap E_g (0.39 eV). The line slope is equal to the defect charge state. The defect chemistry is such that (1) E_F is pinned close to the midgap with almost intrinsic charge carrier concentrations, and (2) the high $\Delta H_{D,q}$ of native defects allow the possibility of introducing effective extrinsic dopants with $\Delta H_{D,q}$ lower than ~0.3 eV for acceptors (ΔE_{acc}) and ~0.5 eV for donors (ΔE_{don}).

In Figure 4, the predominant native defects are the acceptor V_K, the donor Sb_{Ga}, and neutral $Ga_{Sb(4)}$, where Sb(4) represents one of the 4 unique Sb Wyckoff positions in $KGaSb_4$. Unlike many other Zintls,[22] the defect chemistry of $KGaSb_4$ is unique in that the defect formation enthalpies are rather high;

consequently, the defect concentrations are low. Our calculations indicate that the equilibrium carrier concentration in undoped $KGaSb_4$ (300 °C) is approximately 8×10^{13} $e^- cm^{-3}$. While the absolute value of the carrier concentration may not be precise, it confirms the intrinsic nature of undoped $KGaSb_4$. Since Ga_{Sb} (regardless of Wyckoff position) is in neutral state, it does not contribute to charge neutrality. The acceptor V_K and donor Sb_{Ga} establish charge neutrality such that the Fermi level is pinned in the mid gap region. Together with the low defect concentrations, the resultant transport behavior is expected to be intrinsic, which is consistent with our experimental results.

The high formation enthalpies $\Delta H_{D,q}$ of native defects in Figure 4 have implications for extrinsic doping of the system. The large energy window ΔE of >0.5 eV (ΔE_{don}) and >0.3 eV (ΔE_{acc}) is favorable for introduction of energetically favorable donor and acceptor dopants, respectively. A donor/acceptor dopant with formation enthalpy lower than the respective energy window will dope $KGaSb_4$ n- or p-type, respectively, without forming compensating pairs with native defects. The degree to which the system is doped n or p-type will, however, depend on the $\Delta H_{D,q}$ of the extrinsic dopant (typically as a substitutional defect). On the basis of the relative size of the energy window ΔE in the defect diagram (Figure 4), we can expect that n-type doping will be easier to achieve in $KGaSb_4$. The possibility of bipolar doping (i.e., dopable both n- and p-type) of $KGaSb_4$ is exciting. Besides interstitial doping in skutterudites and clathrates, $KGaSb_4$ could represent one of the few Zintls can be doped n- and p-type with a traditional substitutional dopant.

Charge Carrier Properties of Ba-doped $KGaSb_4$. In our prior work, we found that Ba successfully dopes $KAlSb_4$ n-type up to the solubility limit of Ba ($x \sim 0.007$).[23] Encouraged by our intrinsic defect structure calculations and prior work on $KAlSb_4$, we attempted Ba doping of $KGaSb_4$. As may be expected from their similar chemistry and identical structures, Ba doping of $KGaSb_4$ is also successful, consistent with Ba_K^+ substitutional defects. Figure 5 demonstrates the trend in carrier concentration as a function of nominal doping concentration at 400 °C. Consistent with the appearance of the secondary phase in XRD and the evolution of precipitates in SEM at Ba concentrations $x \geq 0.020$, Ba doping effectiveness ceases around $x = 0.020$. Assuming a linear relationship between the electron concentration and the nominal doping, we extrapolate that the solubility of Ba in $KGaSb_4$ is $x \sim 0.017$. Assuming that each Ba_K^+ yields one free electron, the observed doping efficiency of Ba in $KGaSb_4$ is approximately 50%. This is consistent with our prior work on Ba-doped $KAlSb_4$ and the relatively low doping efficiency observed in chemically related Zintl compounds such as Zn-doped Ca_3AlSb_4, Na-doped $Ca_5Al_2Sb_6$, and Zn-doped Sr_3GaSb_3.[23,38−40] Note that $KGaSb_4$ possesses a relatively complex band structure (Figure S3) with multiple low lying bands near the band edge. The low doping efficiency may be a consequence of nonparabolicity interfering with the single parabolic band interpretation of Hall effect. Additionally, as the Fermi level is driven toward the conduction band edge, the concentration of compensating, native V_K vacancies is expected to rise, complicating the analysis.
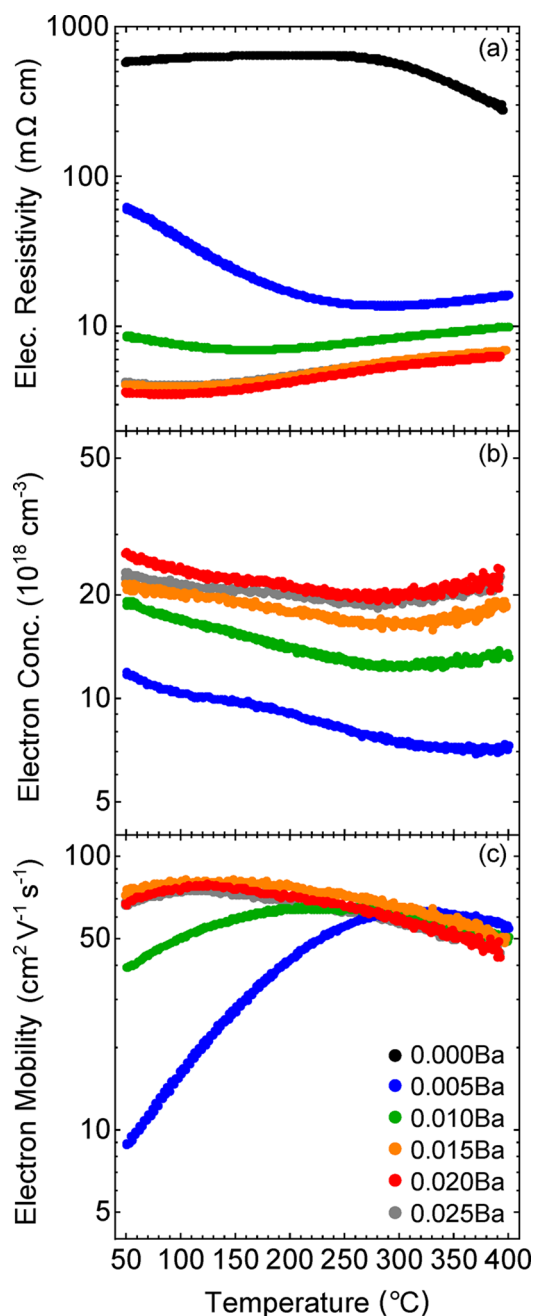
High temperature Hall effect measurements on Ba-doped $KGaSb_4$ yield measurements consistent with the n-type doping of an intrinsic semiconductor. Figure 6 shows the temperature dependence of the electronic resistivity, mobility, and carrier concentration for samples of $K_{1−x}Ba_xGaSb_4$. Note that the
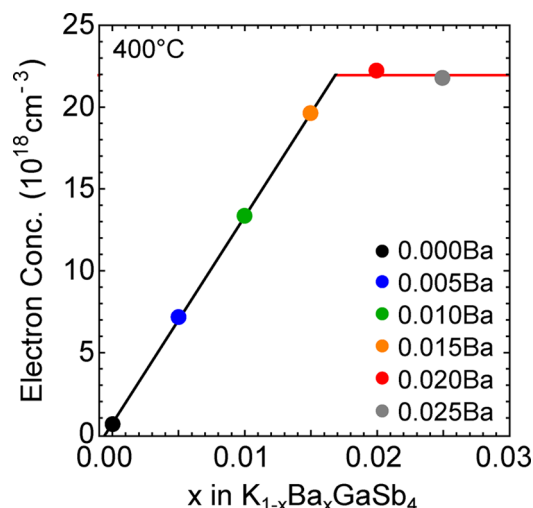
Figure 5. Trend of electron carrier concentration as a function of nominal doping in Ba-doped $KGaSb_4$. We observe that the carrier concentration increases linearly with doping up to the solubility limit (~0.017) of Ba. Termination of doping effectiveness coincides with impurity evolution in both XRD and SEM at Ba concentrations $x \geq 0.020$. Apparent doping effectiveness is approximately 50%. Note that the plot is constructed at 400 °C to coincide with observed max zT.

undoped sample (Figure 3) is only shown in the electrical resistivity (Figure 6a) due to the sign change of the carrier concentration and mobility at high temperatures. The electrical resistivity decreases monotonically up to the solubility limit of Ba. Similar to prior work on $KAlSb_4$, the electrical resistivity and mobility at low temperatures is strongly temperature dependent. However, we note that the magnitude of the thermally activated transport decreases dramatically with a small increase in carrier concentration. For $x = 0.005$, the resistivity drops approximately an order of magnitude from 50 to 250 °C. In comparison, the $x = 0.015$ sample exhibits almost no activated transport. In our prior work on $KAlSb_4$ we ascribed the activated transport to a combination of grain boundary oxidation and contact resistance. Our previous assertions were supported by similar behavior in samples of Ca_3AlSb_4, Sr_3AlSb_3 and Sr_3GaSb_3.[23,38,40,41] However, neither effect can adequately describe the temperature dependent transport in $KGaSb_4$. Of particular interest is the electron mobility (Figure 6c). The peak mobility at low temperatures *increases* with increased doping levels, despite nominally increased charge center scattering from the doping atoms.

As noted in the experimental methods, the first thermal cycle of Hall effect is performed to allow contact annealing, penetration of a thin oxide layer, and bake-out of the boron nitride coating. The first cycle is essential to obtain repeatable data, as it is common to see greatly increased resistivity for the first 100−200 °C, quickly relaxing to the "nominal" values by 300 °C and remaining at appropriate values for all subsequent cycles. Other transport measurements do not exhibit this difficulty. This behavior is also observed in $KAlSb_4$.[23] We commonly run 3−4 sequential thermal cycles during Hall effect measurements to ensure reproducible data. Past the first cycle, data is completed consistently and with minimal hysteresis. If Hall effect probes are removed from the sample, then the thermal cycles must be repeated to obtain stable transport, indicative of a contact issue. However, the effect is not altered by changing the contact metal or polishing the surface, and experimental I−V curves consistently confirm ohmic contacts.

Figure 6. Hall effect measurements on $K_{1-x}Ba_xGaSb_4$ are consistent with the n-type doping of an intrinsic semiconductor. Measurements on undoped $KGaSb_4$ (black) are only shown for the resistivity measurement (a) due to the sign change associated with the bipolar transition from p-type to n-type transport at high temperature. The carrier concentration (b) increases with nominal Ba concentration and is relatively independent of temperature. Electrical resistivity (a) and electron mobility (c) exhibit strong temperature dependence at low temperatures for lightly doped samples ($x \leq 0.010$), vanishing as the doping level increases. Peak mobility in samples of $KGaSb_4$ actually increases with doping level at low temperatures before decaying classically at high temperatures.

We are actively working on growth of single crystals of $KAlSb_4$ and $KGaSb_4$ to eliminate the influence of grain boundaries and crystallographic orientation on the electronic transport.

Figure 7 shows the temperature dependent Seebeck coefficient for samples of $K_{1-x}Ba_xGaSb_4$. Seebeck coefficient measurements on $K_{1-x}Ba_xGaSb_4$ are consistently negative, in
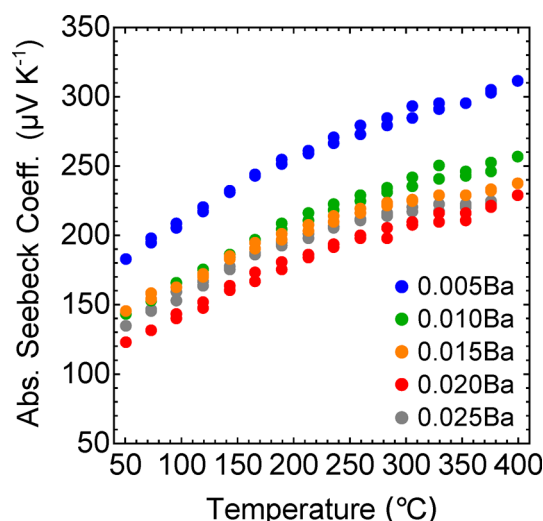

Figure 7. Seebeck coefficient measurements on $K_{1-x}Ba_xGaSb_4$ are consistent with n-type doping of a nominally instrinsic semiconductor. Note that the undoped sample is not shown due to bipolar transport leading to a sign change at high temperatures. For all phase pure samples (Ba $x \leq 0.020$), the Seebeck coefficient decreases monotonically with increasing Ba content, consistent with the behavior of a moderately doped semiconductor.

agreement with n-type doping via Ba_K^+. The Seebeck coefficient of the doped series decreases with increasing Ba content, as expected for a moderately doped semiconductor. We note that the Seebeck coefficient displays an unusual feature at ~350 °C. The values appear to plateau around 300−350 °C before beginning to rise again for temperatures >350 °C. This feature is present in all n-type samples, including a series sent to collaborators at Northwestern University for validation. This effect was not observed in prior work on Ba-doped $KAlSb_4$.[23] Several samples were measured to 500 °C, and while the Seebeck coefficient continues to rise, stability in Hall effect is significantly reduced, limiting the maximum temperature explored in this work. We hypothesize that the increase in the Seebeck coefficient may be related to the unique band-structure of $KGaSb_4$, which contains several low-lying bands near the band edge (see Figure S3). Specifically, we hypothesize that as the Fermi energy moves toward the conduction band edge at high temperatures, the influence of the band at the Z-point (in addition to the primary band edge at the Γ-point) may begin to influence the overall Seebeck coefficient.

To investigate the effect of doping specifically on the Seebeck coefficient, we constructed the Pisarenko diagram for Ba doped $KGaSb_4$ at 400 °C (Figure 8). We model the effect of doping on the Seebeck coefficient in $KGaSb_4$ by solving the Boltzmann transport equation (BTE) within the relaxation time approximation for the Seebeck coefficient S as a function of the reduced chemical potential η (eq 3). For ease of comparison with other thermoelectric work, we assume the system adheres to the single parabolic band model (SPB). However, due to the quasi-2D nature of the band structure surrounding Γ, care must be taken when drawing conclusions from the SPB model. By performing the calculation at elevated temperatures (400 °C), we assume that acoustic phonon scattering is the dominant scattering mechanism (allowing $\lambda = 0$).The full form of the Fermi integral $F(\eta)$ is given by eq 4 where ξ is the reduced carrier energy.[42]
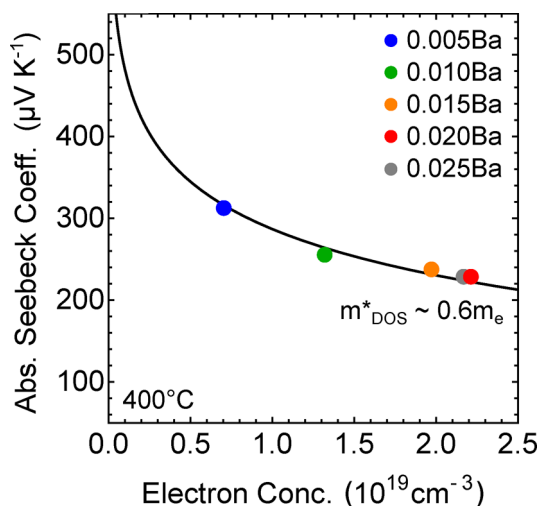
Figure 8. Pisarenko plot of $K_{1-x}Ba_xGaSb_4$ generated using the single parabolic band (SPB) model to fit experimental data with the density of states effective mass (m^*_{DOS}) as the only free parameter. We obtain $m^*_{DOS} \sim 0.6\ m_e$ for Ba doped KGaSb$_4$. Note that the Pisarenko plot is constructed at 400 °C. Undoped KGaSb$_4$ is not included in the data due to the bipolar transport observed at high temperatures.

$$S(\eta) = \frac{k_b}{e} \frac{(2+\lambda)F_{1+\lambda}(\eta)}{(1+\lambda)F_\lambda(\eta)} - \eta \tag{3}$$

$$F_{1+\lambda}(\eta) = \int_0^\infty \frac{\xi^{1+\lambda}}{1+e^{\xi-\eta}}\,d\xi \tag{4}$$

We can now define the carrier concentration as a function of the reduced chemical potential and the density of states (DOS) effective mass m^*_{DOS} (eq 5):

$$n = 4\pi \left(\frac{2m^*_{DOS}k_b T}{h^2}\right)^{3/2} F_{1/2}(\eta) \tag{5}$$

where n is the carrier concentration, T is the temperature, k_b is the Boltzmann constant, and h is Planck's constant.

Equations 3 and 4 generate the Seebeck coefficient S as a function of the chemical potential η. Equation 5 allows us to write η as a function of carrier concentration n and m^*_{DOS}. Thus, we obtain a form for the Seebeck coefficient as a function of the carrier concentration which can be fit to the experimental data with m^*_{DOS} as the only free parameter. For KGaSb$_4$, we find $m^*_{DOS} \sim 0.6\ m_e$. Note that undoped KGaSb$_4$ is not included in the data as the temperature dependent Seebeck coefficient measurements indicate a significant contribution from bipolar effects. We acknowledge the limitations of the SPB model, particularly with a material with a nontrivial band structure. However, the SPB model is widely known and widely applied within the thermoelectric community and thus serves as a useful proxy for comparison with other work.

Extrinsic Defect Calculations and Bipolar Doping. We have seen experimental evidence that Ba serves as an effective dopant in KGaSb$_4$ via Hall effect and Seebeck coefficient measurements. Computation was able to suggest that the lack of energetically favorable intrinsic defects provides a window for a successful extrinsic defect. Ultimately, however, we aim to integrate computation as a *predictive* tool for examining intrinsic and extrinsic defects. To this end, we used the intrinsic defect calculation and experimental survey of other extrinsic dopants

to examine ex post facto the success of extrinsic defect calculations in structurally complex systems.

We experimentally synthesized samples of KGaSb$_4$ with a variety of n-type (Ba, Sr, Ca, Te) and p-type (Zn, Sn) dopants. Ba (n-type) and Zn (p-type) doping were both successful in significantly changing the carrier concentration. Ba was by far the most effective, yielding an increase of approximately 10^{19} e$^-$cm^{-3} for each 1% substitution. While Zn was successful in doping KGaSb$_4$ p-type, it was only was moderately effective, yielding 5×10^{18} h$^+$cm^{-3} for each 1% nominal substitution. The effectiveness of Zn as a p-type dopant is well documented in chemically related Zintl compunds, presumably from the substitution of Zn on the group III (Al, Ga, In) elements. We note that in many related Zintl compounds, Zn often exhibits somewhat reduced doping efficiency.[28,40,43,44] Despite chemical similarity to Ba and a similar ionic radius with K, Sr doping failed to significantly increase the electron concentration and exhibited limited experimental solubility due to the presence of a competing phase. Both Ca and Te negatively impacted the stability of KGaSb$_4$ and were not considered further. Sn appears to be soluble in KGaSb$_4$ but is ineffective in altering the carrier concentration from intrinsic conditions.

Given the experimental results, we used first-principles defect calculations to understand the effectiveness of Ba and Sr as n-type dopants and Zn as p-type dopant. Figure 9 shows the
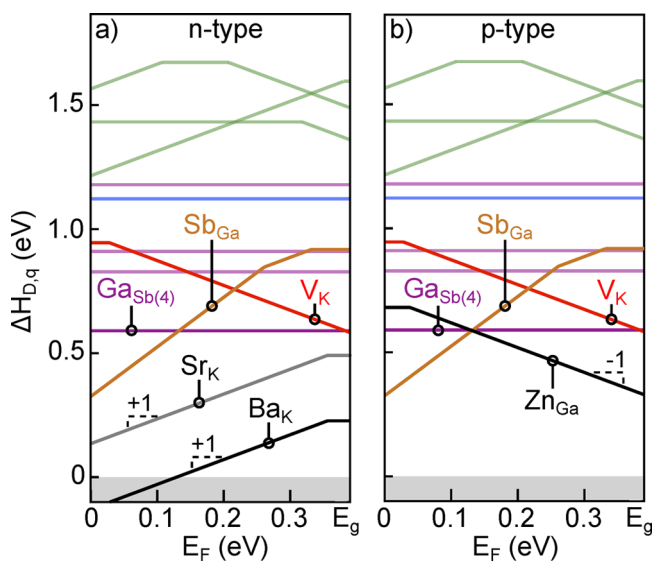
Figure 9. Defect diagrams for p-type and n-type dopants of interest in KGaSb$_4$ are shown with the formation enthalpy $\Delta H_{D,q}$ as a function of Fermi level E_F. The lowest energy native defects in KGaSb$_4$ are also shown for reference (Figure 4). a) The low $\Delta H_{D,q}$ of Ba$_K$ and the absence of Fermi level pinning suggests that Ba is an effective n-type dopant for KGaSb$_4$. The relatively higher formation energy for Sr$_K$ confirms that Sr should be a poor dopant when compared to Ba. b) The high $\Delta H_{D,q}$ of Zn$_{Ga}$ leads to intersection with Sb$_{Ga}$ antisite defects and therefore, Fermi level pinning. The corresponding low hole concentration suggests that Zn is an ineffective p-type dopant.

defect calculations for Ba, Sr, and Zn as substitutional dopants. The formation enthalpies of native defects are also shown in Figure 9. For clarity, only the lowest-energy substitutional defect for each dopant is shown (we calculated $\Delta H_{D,q}$ for all sites).

Figure 9a shows the defect formation enthalpies of Ba$_K$ and Sr$_K$ in KGaSb$_4$. Our calculations find that both Ba$_K$ and Sr$_K$

possess $\Delta H_{D,q}$ smaller than ΔE_{don} (Figure 4) suggesting that both Ba and Sr are be potential candidates for n-type doping. The Ba_K defect is has a particularly low formation enthalpy, placing it well below the influence of the lowest possible compensating defect, Sb_{Ga}. Furthermore, the much lower $\Delta H_{D,q}$ of Ba_K when compared to Sr_K is responsible for the much higher doping effectiveness of Ba in the experimental survey (i.e., higher Hall electron concentration). Our computations similarly find that the influence of Ba should be approximately 2 orders of magnitude higher than that of Sr (6×10^{20} e$^-$cm^{-3} vs 3×10^{18} e$^-$cm^{-3}, respectively). Again, while the absolute values for the carrier concentration calculations are not expected to be true to experiment, their relative values are consistent with Hall effect measurements on Ba and Sr doped $KGaSb_4$.

For p-type doping with Zn, we find that the Zn_{Ga} substitutional defect is the lowest-energy defect (Figure 9a). However, unlike Ba_K and Sr_K (Figure 9a), the action of Zn_{Ga} is compensated by formation of the native defect Sb_{Ga}. The acceptor-donor defect compensation pins the Fermi level (E_F) in the lower half of the gap, resulting in a lightly p-doped system. Ultimately, the E_F pinning is responsible for the lower effectiveness of p-type doping with Zn. Consistent with the experimental results, Zn doping at maximum solubility yields a weakly p-type material. It is worth noting that the defect diagrams are drawn explicitly for the region of phase stability (K−Ga−Sb−X, X = Ba, Sr, Zn) corresponding to the most X-rich conditions without thermodynamically destabilizing the $KGaSb_4$ phase. This essentially draws the plots at the effective solubility limit of the extrinsic dopant. Specifically, for Zn doping, note that the formation enthalpy of Zn_{Ga} is higher than the corresponding Ba_K and Sr_K dopants, indicating a lower solubility of Zn in $KGaSb_4$. We observe that the solubility of Ba is <1.7 mol %, so it is likely that the 1 mol % Zn substitution used here already approaches the effective solubility of Zn in $KGaSb_4$.

Our defect calculations reveal that the effectiveness of extrinsic doping is driven by the energetics of the charged native defects (Sb_{Ga}, V_K) and the thermodynamics of phase stability in the quaternary K−Ga−Sb−X (where X = Ba, Sr, Zn) phase space. Through first-principles defect calculations, we now understand the underlying defect physics that is responsible for the effective n-type doping with Ba and the diminished doping efficiency of Zn. The agreement between experiments and computations allows us to place greater confidence in future computational results ex ante facto in addition to ex post facto.

Thermal Properties. The thermal properties of $KGaSb_4$ are near identical to those observed in $KAlSb_4$.[23] The thermal diffusivity of $KGaSb_4$ was measured to 400 °C. The total thermal conductivity is calculated using the Debye−Callaway approximation for the volumetric heat capacity and can be found in Figure S4. As expected, total thermal conductivity increases with doping concentration due to increased contributions from the electronic thermal conductivity. To decouple the electronic contribution to the thermal conductivity from the lattice and bipolar contributions, the Wiedemann−Franz relationship $\kappa_e = LT/\rho$ is used. The Lorenz number L is calculated within the SPB model according to eq 6.[42]

$$L = \left(\frac{k_b}{e}\right)^2 \frac{(1 + \lambda)(3 + \lambda)F_\lambda(\eta)F_{\lambda+2}(\eta) - (2 + \lambda)^2 F_{\lambda+1}(\eta)^2}{(1 + \lambda)^2 F_\lambda(\eta)^2}$$

(6)

where the reduced chemical potential η is calculated from the experimentally observed Seebeck coefficients according to eq 3. Again we assume that scattering is dominated by acoustic phonon scattering ($\lambda = 0$). However, we acknowledge that the low temperature electronic transport has significant contributions from the activated transport which will increase error in the calculation of the lattice thermal conductivity at low temperatures. The calculated Lorenz numbers for all samples can be found in Figure S5. We find that the electronic contribution to the thermal conductivity is relatively low (≤ 0.1 Wm^{-1}K^{-1}) for most temperatures and compositions. Subtracting the electronic contribution from the thermal conductivity results in the curves seen in Figure 10. Only the undoped
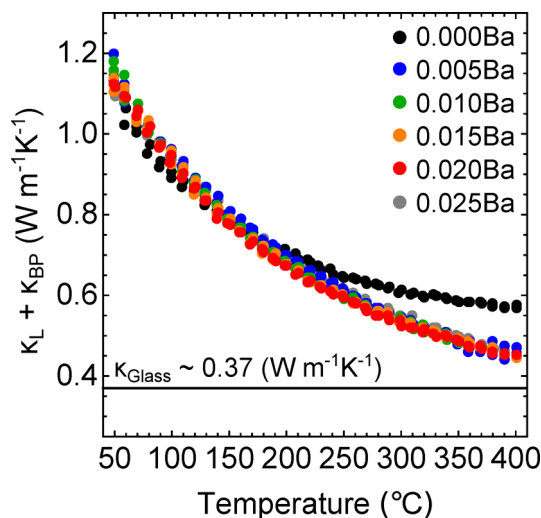
Figure 10. Lattice thermal conductivity in doped samples is unchanged with respect to Ba concentration. Intrinsic $KGaSb_4$ exhibits a strong bipolar contribution beyond 200 °C, consistent with an undoped, small-gap semiconductor. Onset of bipolar behavior coincides with the bipolar transport in both the Seebeck coefficient and Hall carrier concentration measurements for the undoped sample. The subtracted electronic contribution to the thermal conductivity is relatively small, ∼ 0.1 Wm^{-1}K^{-1}. The lattice thermal conductivity for $KGaSb_4$ approaches the glassy minimum, estimated to be ∼0.37 Wm^{-1}K^{-1}.

sample demonstrates a significant bipolar contribution at temperatures >200 °C, which roughly coincides with the emergence of the bipolar transport in both the Seebeck coefficient and Hall carrier concentration for undoped $KGaSb_4$ (Figure 3). Due to the low concentration of Ba and the similarity of the Ba and K ionic radii, we see little to no change in the lattice thermal conductivity as a function of Ba concentration.

The asymptotic form of the high temperature thermal conductivity can be estimated using the high temperature limit of the spectral heat capacity within the Debye−Callaway model. Assuming that $KGaSb_4$ exhibits glass-like thermal conductivity, we can obtain an estimate for the temperature independent glassy limit, eq 7.[45]

$$\kappa_{\text{Glass}} = \frac{3k_b v_g}{2V^{2/3}} \left(\frac{\pi}{6}\right)^{1/3}$$

(7)

where k_b is the Boltzmann constant. We approximate the phonon group velocity v_g by the average speed of sound ($v_g(\omega) \sim v_s$). Ultrasonic measurements performed on $KGaSb_4$ find that

$v_{Long} \sim 3090m/s$ and $v_{Shear} \sim 1840m/s$, which yields an average speed of sound of $v_s \sim 2250m/s$. The speed of sound in $KGaSb_4$ is consistent with chemically similar Zintl compounds $KAlSb_4$, $Ca_5Al_2Sb_6$, Sr_3GaSb_3, Sr_3AlSb_3, and Ca_3AlSb_3.[23,38−41] For $KGaSb_4$, we find the glassy contribution specifically from optical modes to be $\sim 0.33 Wm^{-1}K^{-1}$.

We attempted to model the temperature dependence of $KGaSb_4$ with the Debye−Callaway model,[45] but found that the model could not reproduce the functional form of the experimental data without changing the temperature dependence of the Umklapp scattering term. The addition of boundary scattering and point defect scattering does not improve the model. Growth of single crystal $KGaSb_4$ is ongoing to better characterize anisotropy and anharmonicity in this system.

Figure of Merit. The themoelectric figure of merit, zT, for samples of $K_{1-x}Ba_xGaSb_4$ is shown in Figure 11. We find that a
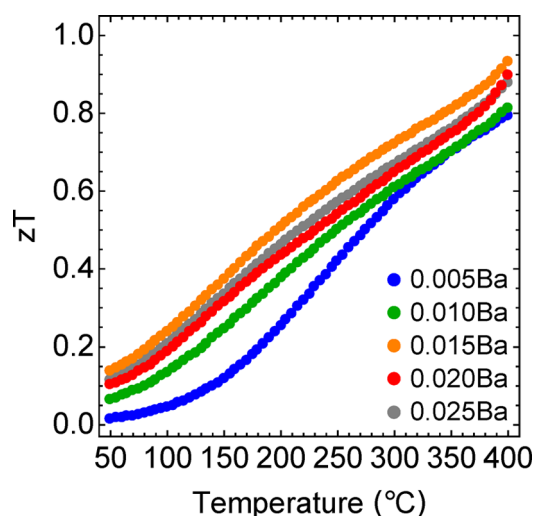
Figure 11. High temperature zT exceeds 0.9 at 400 °C for samples doped with 1.5 mol % Ba. It is worth noting that all samples, regardless of dopant concentration, exceed $zT \sim 0.8$. We do not observe a peak in zT up to 400 °C, driven by a continually increasing Seebeck coefficient. High temperature measurements are limited by the stability of $KGaSb_4$ during Hall effect measurements. If stability can be improved, $zT > 1$ should be readily obtainable in this system.

maximum zT value of 0.92 is obtained at 400 °C for nominal composition $K_{0.895}Ba_{0.015}GaSb_4$. We note that the effect of doping is relatively weak in samples of $KGaSb_4$, as all samples, regardless of doping, have $zT > 0.8$ at 400 °C. Driven by the increasing Seebeck coefficient at high temperatures, we do not see a peak in zT by 400 °C. While Seebeck effect and thermal conductivity measurements can be made above 400 °C, we note significant stability issues during Hall effect measurements at higher temperatures. Above 450 °C, samples of $KGaSb_4$ begin to exhibit signs of sublimation. Our collaborators also note deleterious reactions with their alumina sample holder at 500 °C. We have been conservative with our maximum temperature for this work, but if high-temperature stability can be improved in $KGaSb_4$, $zT > 1$ should be easily achievable.

Properties of $KGaSb_4$–$KAlSb_4$ Alloys. Within thermoelectrics, optimization of a new material system is critical to its success. Doping is the primary concern, which we have thoroughly investigated within $KAlSb_4$ and $KGaSb_4$. However, the introduction of point defect scattering via alloying is another technique commonly used to improve the thermo-

electric performance of new materials. In our prior work on $KAlSb_4$, we identified that the n-type band edge is composed primarily of Sb p-states and Sb s-states. We hypothesized that alloying on either the K or Al sites could result in reduced thermal conductivity while leaving the electronic mobility largely unchanged. With $KGaSb_4$ also proving a strong thermoelectric material, and spurred by our prior work, we investigated the solid solution series $KGa_{1-x}Al_xSb_4$.

Barium has proven an effective dopant in both systems; to ensure reliable Hall effect measurements, all samples were doped with 1% Ba. In prior work, we identified that $KAlSb_4$ is best grown with a deficiency of Sb to suppress Sb impurities. As such, we adopted a set growth condition corresponding to $K_{0.99}Ba_{0.01}Al_{1-x}Ga_xSb_{3.80}$ (hereby referred to as KGAS), where x = (0, 0.1, 0.3, 0.5, 0.7, 0.9, 1.0).

To confirm solubility of Ga on the Al site, we performed X-ray diffraction and Rietveld refinement on sintered samples of KGAS to generate Figure 12. We observe the *full solid solution*
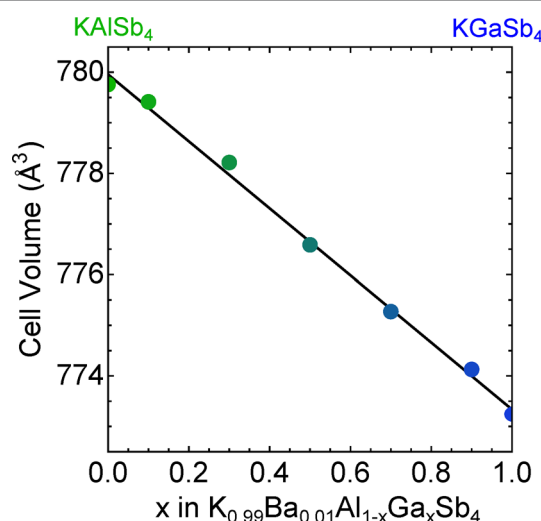
Figure 12. Cell volume as a function of Ga concentration in alloys of $KAlSb_4$ and $KGaSb_4$. As expected by Vegard's Law, cell volume trends linearly with alloying concentration. Unintuitively, $KGaSb_4$ actually possesses a smaller cell volume when compared to $KAlSb_4$. No phase separation into the constituent ternary phases is observed over the composition range, consistent with the Rietveld refinement. Minor impurities of $KGaSb_2$ are present for Ga > 50%, although the impurities are directly related to the Sb-poor growth conditions, and do not indicate limited solubility of $KAlSb_4$ in $KGaSb_4$.

of $KAlSb_4$ and $KGaSb_4$, consistent with the identical structure types and similar lattice constants. Contrary to intuition, we observe that $KGaSb_4$ is actually smaller than $KAlSb_4$. The smaller cell volume of $KGaSb_4$ is consistent with the original structural refinements of $KAlSb_4$ and $KGaSb_4$, but is not well understood.[26,46] We note that samples with Ga > 50% begin to exhibit a small percentage of $KGaSb_2$ as a secondary phase. This is expected, as the synthesis of $KGaSb_4$ does not require the Sb-deficient conditions that $KAlSb_4$ necessitates. No other secondary phases are observed. All XRD results can be found in Figure S8.

Figure 13 demonstrates the lattice thermal conductivity and intrinsic mobility (obtained via the single parabolic band model) for the KGAS alloys. Results for the lattice thermal conductivity are given at both 50 and 400 °C. The intrinsic mobility is only calculated at 400 °C as samples rich in Al
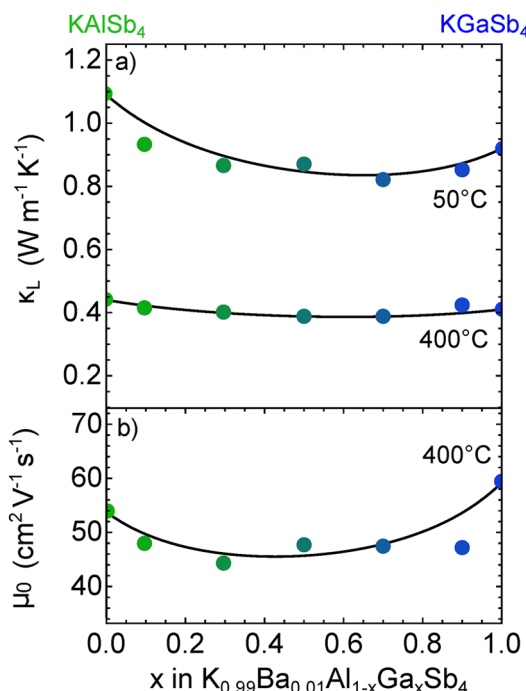
Figure 13. Trends in lattice thermal conductivity κ_L (a) and intrinsic electron mobility μ_0 (b) as a function of alloying composition. While a decrease (relative to the pure end points) is observed in the lattice thermal conductivity at room temperature, there is a negligible depression of lattice thermal conductivity at 400 °C. The intrinsic mobility decreases by ~20% due to alloying. Due to the minimal effect on the lattice thermal conductivity, the decrease in mobility causes a loss of thermoelectric potential l over all compositions relative to pure KGaSb$_4$.

exhibit the activated low temperature transport observed in our prior work.[23] To further investigate the composition dependent transport in KGAS, we applied the point defect scattering model proposed by Abeles.[47] The Abeles model has been applied in many thermoelectric systems to date including the half-Heuslers, skutterudites, Si$_{1-x}$Ge$_x$, and SnSe.[47−51] This model predicts that the depression in the lattice thermal conductivity from point defects can be modeled approximately by eq 8:

$$\kappa_{L,(A,B)}(x) \propto \left((1-x)\kappa_{0,A} - x\kappa_{0,B}\right)\frac{\arctan\left((x(1-x))^{1/2}\right)}{(x(1-x))^{1/2}}$$

$$(8)$$

where $\kappa_{L,(A,B)}(x)$ is the predicted lattice thermal conductivity of an alloy between A and B as a function of alloying fraction x (e.g., $A_{1-x}B_x$). The lattice thermal conductivity of pure A and pure B is given by $\kappa_{0,A}$ and $\kappa_{0,B}$, respectively. The solid line in Figure 13a represent the Abeles approximation for the experimental thermal conductivity data. The solid line in Figure 13b represents a similar fit for the mobility where the intrinsic mobilities of the pure end points were substituted into eq 8.

We observe that while the thermal conductivity (Figure 13a) decreases significantly (~30%) at room temperature, transport at 400 °C is largely unaffected. As KAlSb$_4$ and KGaSb$_4$ are already near the "glassy minimum" at 400 °C before alloying, the substitution of Al on Ga has a minimal effect. Conversely, although the intrinsic mobility is not severely depressed, we still suffer ~20% loss of mobility by 50% substitution. It is

important to note that the KGaSb$_2$ impurity in the Ga-rich samples did have deleterious effect on the mobility when compared with the phase-pure samples from the Ba doping series in Figure 6. While this could potentially affect the analysis, it is important to recall that there is a negligible decrase in thermal conductivity at 400 °C; thus, *any* decrease in mobility will result in a net loss of thermoelectric potential.

Both KAlSb$_4$ and KGaSb$_4$ are mobility driven systems, and while the loss of mobility is not severe (~20%), the decrease in thermal conductivity at high temperatures is not large enough to compensate. As a result, the net thermoelectric potential of the alloyed system decreases. As a result, we did not perform carrier concentration optimization on any of the alloyed compositions. Near glassy thermal conductivity at high temperature is typical of Zintl materials. Thus, the impact of isoelectronic alloying on the thermal transport is not as dramatic as in high κ_L systems. These results highlight the need to focus on the intrinsic electronic properties for further optimization.

CONCLUSIONS

In this work, we have experimentally investigated the thermoelectric potential for n-type KGaSb$_4$ doped with Ba. We also applied a series of first-principles defect calculations to understand the underlying defect chemistry that enables n-type transport in KGaSb$_4$. We first examined the experimental transport properties in undoped KGaSb$_4$, finding that KGaSb$_4$ is a lightly compensated, intrinsic semiconductor. We discovered that the substitutional doping of Ba on the K site is quite effective as a donor defect. A combination of XRD, Hall effect measurements, and electron microscopy revealed that the solubility of Ba in KGaSb$_4$ is approximately 1.7 mol %, which corresponds to a doping level of approximately 2.2×10^{19} e$^-$cm^{-3}. Combined with the extremely low lattice thermal conductivity (~0.5 Wm^{-1}K^{-1}), a relatively high electron mobility (~50 cm^2 V^{-1}s^{-1}) yields $zT > 0.9$ at 400 °C. Furthermore, zT is still rising rapidly at 400 °C, suggesting that $zT > 1$ should be easily achievable if the high temperature stability during Hall measurements can be improved. We also briefly discussed the solid-solution KGa$_{1-x}$Al$_x$Sb$_4$, where we found full solubility between KGaSb$_4$ and KAlSb$_4$, although the thermoelectric potential was not improved.

The relative scarcity of n-type Zintl literature prompted us to explore the fundamental defect structure that allows KGaSb$_4$ to be doped n-type. First-principles calculations reveal that no dominant intrinsic defects are present to drive the structure to either a n-type or p-type carrier type. Consistent with experiment, computations found that Ba should act as a successful n-type dopant. We also investigated the potential for bipolar doping in KGaSb$_4$, finding that the material is also successfully doped p-type with Zn (~5 × 10^{18} h$^+$cm^{-3} at 1 mol %). However, the compensating native defect Sb$_{Ga}$ limits the effectiveness of Zn as a p-type dopant. This represents one of the few instances of a bipolar dopable Zintl compound and one of the first that does not require interstitial doping to accomplish this (as opposed to skutterudites and clathrates). The minimal role of V$_K$ (commonly assumed to be the source of p-type behavior in Zintl compounds) suggests that chemical intuition is limited even on the most basic level and highlights the need for calculations.

AUTHOR INFORMATION

Corresponding Authors

*E-mail: bortiz@mines.edu (B.R.O.).
*E-mail: etoberer@mines.edu (E.S.T.).

ORCID ⓘ

Brenden R. Ortiz: 0000-0002-1333-7003

Notes

The authors declare no competing financial interest.

REFERENCES

(1) Snyder, G. J.; Toberer, E. S. Complex Thermoelectric Materials. *Nat. Mater.* **2008**, *7*, 105−114.

(2) Baranowski, L.; Snyder, G. J.; Toberer, E. S. Concentrated Solar Thermoelectric Generators. *Energy Environ. Sci.* **2012**, *5*, 9055−9067.

(3) Bell, L. Cooling, Heating, Generating Power, and Recovering Waste Heat with Thermoelectric Systems. *Science* **2008**, *321*, 1457−1461.

(4) Carrete, J.; Mingo, N.; Wang, S.; Curtarolo, S. Nanograined Half-Heusler Semiconductors as Advanced Thermoelectrics: An Ab Initio High-Throughput Statistical Study. *Adv. Funct. Mater.* **2014**, *24*, 7427−7432.

(5) Zhang, Y.; Skoug, E.; Cain, J.; Ozoliņš, V.; Morelli, D.; Wolverton, C. First-Principles Description of Anomalously Low Lattice Thermal Conductivity in Thermoelectric Cu-Sb-Se Ternary Semiconductors. *Phys. Rev. B: Condens. Matter Mater. Phys.* **2012**, *85*, 054306.

(6) Opahle, I.; Parma, A.; McEniry, E. J.; Drautz, R.; Madsen, G. K. H. High-Throughput Study of the Structural Stability and Thermoelectric Properties of Transition Metal Silicides. *New J. Phys.* **2013**, *15*, 105010.

(7) Opahle, I.; Madsen, G. K. H.; Drautz, R. High Throughput Density Functional Investigations of the Stability, Electronic Structure and Thermoelectric Properties of Binary Silicides. *Phys. Chem. Chem. Phys.* **2012**, *14*, 16197−16202.

(8) Zhu, H.; Hautier, G.; Aydemir, U.; Gibbs, Z. M.; Li, G.; Bajaj, S.; Pohls, J.-H.; Broberg, D.; Chen, W.; Jain, A.; White, M. A.; Asta, M.; Snyder, G. J.; Persson, K.; Ceder, G. Computational and Experimental Investigation of TmAgTe₂ and XYZ₂ Compounds, a New Group of Thermoelectric Materials Identified by First-Principles High-Throughput Screening. *J. Mater. Chem. C* **2015**, *3*, 10554−10565.

(9) Yan, J.; Gorai, P.; Ortiz, B. R.; Miller, S.; Barnett, S. A.; Mason, T.; Stevanović, V.; Toberer, E. S. Material Descriptors for Predicting Thermoelectric Performance. *Energy Environ. Sci.* **2015**, *8*, 983−994.

(10) Chasmar, R. P.; Stratton, R. *The Thermoelectric Figure of Merit and Its Relation to Thermoelectric Generators*; Research series; Metropolitan Vickers Electrical, 1959.

(11) Pei, Y.; Gibbs, Z. M.; Gloskovskii, A.; Balke, B.; Zeier, W. G.; Snyder, G. J. Optimum Carrier Concentration in n-Type PbTe Thermoelectrics. *Phys. Rev. B: Condens. Matter Mater. Phys.* **1998**, *57*, 1505−1509.

(12) Bhattacharya, S.; Gunda, N. S. H.; Stern, R.; Jacobs, S.; Chmielowski, R.; Dennler, G.; Madsen, G. K. H. Achieving Optimum Carrier Concentrations in p-Doped SnS Thermoelectrics. *Phys. Chem. Chem. Phys.* **2015**, *17*, 9161−9166.

(13) Zhao, L. D.; Zhang, X.; Wu, H.; Tan, G.; Pei, Y.; Xiao, Y.; Chang, C.; Wu, D.; Chi, H.; Zheng, L.; Gong, S.; Uher, C.; He, J.; Kanatzidis, M. G. Enhanced Thermoelectric Properties in the Counter-Doped SnTe system with Strained Endotaxial SrTe. *J. Am. Chem. Soc.* **2016**, *138*, 2366−2373.

(14) Toberer, E. S.; Brown, S. R.; Ikeda, T.; Kauzlarich, S. M.; Snyder, J. G. High Thermoelectric Efficiency in Lanthanum Doped Yb₁₄MnSb₁₁. *Appl. Phys. Lett.* **2008**, *93*, 062110.

(15) Ballikaya, S.; Chi, H.; Salvador, J. R.; Uher, C. Thermoelectric Properties of Ag-doped Cu₂Se and Cu₂Te. *J. Mater. Chem. A* **2013**, *1*, 12478−12484.

(16) Goyal, A.; Gorai, P.; Peng, H.; Lany, S.; Stevanović, V. A Computational Framework for Automation of Point Defect Calculation. *Comput. Mater. Sci.* **2017**, *130*, 1−9.

(17) Deml, A. M.; Holder, A. M.; O'Hayre, R. P.; Musgrave, C. B.; Stevanović, V. Intrinsic Material Properties Dictating Oxygen Vacancy Formation Energetics in Metal Oxides. *J. Phys. Chem. Lett.* **2015**, *6*, 1948−1953.

(18) Martinez, A. D.; Warren, E. L.; Gorai, P.; Borup, K. A.; Kuciauskas, D.; Dippo, P. C.; Ortiz, B. R.; Macaluso, R. T.; Nguyen, S. D.; Greenaway, A. L.; Boettcher, S. W.; Norman, A. G.; Stevanović, V.; Toberer, E. S. Solar Energy Conversion Properties and Defect Physics of ZnSiP₂. *Energy Environ. Sci.* **2016**, *9*, 1031−1041.

(19) Kosyak, V.; Amiri, N. B. M.; Postnikov, A. V.; Scarpulla, M. A. Model of Native Point Defect Equilibrium in Cu₂ZnSnS₄ and Application to One-Zone Annealing. *J. Appl. Phys.* **2013**, *114*, 1−13.

(20) Yildirim, H.; Kinaci, A.; Chan, M. K. Y.; Greeley, J. P. First-Principles Analysis of Defect Thermodynamics and Ion Transport in Inorganic SEI Compounds: LiF and NaF. *ACS Appl. Mater. Interfaces* **2015**, *7*, 18985−18996.

(21) Pomrehn, G. S.; Zevalkink, A.; Zeier, W. G.; van de Walle, A.; Snyder, G. J. Defect-Controlled Electronic Properties in AZn₂Sb₂ Zintl Phases. *Angew. Chem., Int. Ed.* **2014**, *53*, 3422−3426.

(22) Bjerg, L.; Madsen, G. K. H.; Iversen, B. B. Ab Initio Calculations of Intrinsic Point Defects in ZnSb. *Chem. Mater.* **2012**, *24*, 2111−2116.

(23) Ortiz, B. R.; Gorai, P.; Krishna, L.; Mow, R.; Lopez, A.; McKinney, R.; Stevanović, V.; Toberer, E. S. Potential for High Thermoelectric Performance in n-Type Zintl Compounds: a Case Study of Ba Doped KAlSb₄. *J. Mater. Chem. A* **2017**, *5*, 4036−4046.

(24) Nagu, M. P. Synthesis and Thermoelectric Studies of Zintl Phases in the systems Ba-Al-Sb, Ba-Ga-Sb, and Ba-In-Sb. Ph.D. thesis, The Technical University of Darmstadt, 2014.

(25) Kauzlarich, S. M.; Condron, C. L.; Wassei, J. K.; Ikeda, T.; Snyder, J. G. Structure and High-Temperature Thermoelectric Properties of SrAl₂Si₂. *J. Solid State Chem.* **2009**, *182*, 240−245.

(26) Cordier, G.; Ochmann, H. Crystal Structure of Potassium Tecto-Tetraantimonidogallate, KGaSb₄. *Z. Kristallogr.* **1991**, *195*, 306−307.

(27) Aydemir, U.; Zevalkink, A.; Ormeci, A.; Bux, S.; Snyder, J. G. Enhanced Thermoelectric Properties of the Zintl Phase BaGa₂Sb₂ via Doping with Na or K. *J. Mater. Chem. A* **2016**, *4*, 1867−1875.

(28) Aydemir, U.; Zevalkink, A.; Ormeci, A.; Gibbs, Z. M.; Bux, S.; Snyder, J. G. Thermoelectric Enhancement in BaGa₂Sb₂ by Zn Doping. *Chem. Mater.* **2015**, *27*, 1622−1630.

(29) Toby, B. H.; Von Dreele, R. B. GSAS-II: the Genesis of a Modern Open-Source All Purpose Crystallography Software Package. *J. Appl. Crystallogr.* **2013**, *46*, 544−549.

(30) Borup, K. A.; de Boor, J.; Wang, H.; Drymiotis, F.; Gascoin, F.; Shi, X.; Chen, L.; Fedorov, M. I.; Muller, E.; Iversen, B. B.; Snyder, G. J. Measuring Thermoelectric Transport Properties of Materials. *Energy Environ. Sci.* **2015**, *8*, 423−435.

(31) Iwanaga, S.; Toberer, E. S.; LaLonde, A.; Snyder, G. J. A High Temperature Apparatus for Measurement of the Seebeck Coefficient. *Rev. Sci. Instrum.* **2011**, *82*, 063905.

(32) Kresse, G.; Furthmüller, J. Efficient Iterative Schemes for Ab Initio Total-Energy Calculations Using a Plane-Wave Basis Set. *Phys. Rev. B: Condens. Matter Mater. Phys.* **1996**, *54*, 11169−11186.

(33) Perdew, J. P.; Burke, K.; Ernzerhof, M. Generalized Gradient Approximation Made Simple. *Phys. Rev. Lett.* **1996**, *77*, 3865−3868.

(34) Blöchl, P. E. Projector Augmented-Wave Method. *Phys. Rev. B: Condens. Matter Mater. Phys.* **1994**, *50*, 17953−17979.

(35) Stevanović, V.; Lany, S.; Zhang, X.; Zunger, A. Correcting Density Functional Theory for Accurate Predictions of Compound Enthalpies of Formation: Fitted Elemental-Phase Reference Energies. *Phys. Rev. B* **2012**, *85*, 115104.

(36) Peng, H.; Scanlon, D. O.; Stevanović, V.; Vidal, J.; Watson, G. W.; Lany, S. Convergence of Density and Hybrid Functional Defect Calculations for Compound Semiconductors. *Phys. Rev. B: Condens. Matter Mater. Phys.* **2013**, *88*, 115201.

(37) Lany, S.; Zunger, A. Accurate Prediction of Defect Properties in Density Functional Supercell Calculations. *Modell. Simul. Mater. Sci. Eng.* **2009**, *17*, 084002.

(38) Zevalkink, A.; Toberer, E. S.; Zeier, W. G.; Flage-Larsen, E.; Snyder, G. J. Ca_3AlSb_3: an Inexpensive, Non-Toxic Thermoelectric Material for Waste Heat Recovery. *Energy Environ. Sci.* **2011**, *4*, 510−518.

(39) Toberer, E. S.; Zevalkink, A.; Crisosto, N.; Snyder, J. G. The Zintl compound $Ca_5Al_2Sb_6$ for Low-Cost Thermoelectric Power Generation. *Adv. Funct. Mater.* **2010**, *20*, 4375−4380.

(40) Zevalkink, A.; Zeier, W. G.; Pomrehn, G.; Tremel, W.; Snyder, G. J.; Schechtel, E. Thermoelectric Properties of Sr_3GaSb_3 - a Chain-Forming Zintl Compound. *Energy Environ. Sci.* **2012**, *5*, 9121−9128.

(41) Zevalkink, A.; Pomrehn, G.; Takagiwa, Y.; Swallow, J.; Snyder, G. J. Thermoelectric Properties and Electronic Structure of the Zintl-Phase Sr_3AlSb_3. *ChemSusChem* **2013**, *6*, 2316−2321.

(42) Kim, H.-S.; Gibbs, Z. M.; Tang, Y.; Wang, H.; Snyder, J. G. Characterization of Lorenz Number with Seebeck Coefficient Measurement. *APL Mater.* **2015**, *3*, 041506.

(43) Chanakian, C.; Aydemir, U.; Zevalkink, A.; Gibbs, Z. M.; Fleurial, J.-P.; Bux, S.; Snyder, G. J. High Temperature Thermoelectric Properties of Zn-doped $Eu_5In_2Sb_6$. *J. Mater. Chem. C* **2015**, *3*, 10518−10524.

(44) Chanakian, S.; Zevalkink, A.; Aydemir, U.; Gibbs, Z. M.; Pomrehn, G.; Fleurial, J.-P.; Bux, S.; Snyder, G. J. Enhanced Thermoelectric Properties of $Sr_5In_2Sb_6$ via Zn-doping. *J. Mater. Chem. A* **2015**, *3*, 10289−10295.

(45) Toberer, E. S.; Zevalkink, A.; Snyder, J. G. Phonon Engineering Through Crystal Chemistry. *J. Mater. Chem.* **2011**, *21*, 15843−15852.

(46) Cordier, G.; Ochmann, H. Crystal structure of potassium tecto-tetraantimonidoaluminate, $KAlSb_4$. *Z. Kristallogr.* **1991**, *195*, 308−309.

(47) Abeles, B. Lattice Thermal Conductivity of Disordered Semiconductor Alloys at High Temperatures. *Phys. Rev.* **1963**, *131*, 1906−1911.

(48) Ortiz, B. R.; Peng, H.; Lopez, A.; Parilla, P. A.; Lany, S.; Toberer, E. S. Effect of Extended Strain Fields on Point Defect Phonon Scattering in Thermoelectric Materials. *Phys. Chem. Chem. Phys.* **2015**, *17*, 19410−19423.

(49) Yang, J.; Li, H.; Wu, T.; Zhang, W.; Chen, L.; Yang, J. Evaluation of Half-Heusler Compounds as Thermoelectric Materials Based on the Calculated Electrical Transport Properties. *Adv. Funct. Mater.* **2008**, *18*, 2880−2888.

(50) Zhou, M.; Chen, L.; Zhang, W.; Feng, C. Disorder Scattering Effect on the High-Temperature Lattice Thermal Conductivity of TiCoSb-Based Half-Heusler Compounds. *J. Appl. Phys.* **2005**, *98*, 013708.

(51) Zhou, Z.; Uher, C.; Jewell, A.; Caillat, T. Influence of Point-Defect Scattering on the Lattice Thermal Conductivity of Solid Solution $Co(Sb_{1−x}As_x)_3$. *Phys. Rev. B* **2005**, *71*, 235209.